ENGINEERING Energy 2026, 20(2): 1067z
https://doi.org/10.1007/s11708-026-1067-z

RESEARCH ARTICLE

Localization of high-entropy metal oxide in iron oxide nanoparticles for efficient oxygen evolution reaction

Liang Qiu[1#], Baowen Zhou (✉)[1#], Ying Li[2], Muhammad Imran Abdullah[2], Zhaosong Wu[1], Jianqing Chen[1], Wanglan Zhou[1], Tingting Ren[3], Yuqi Wang[3], Zhen Huang[1]

1 Key Laboratory for Power Machinery and Engineering of the Ministry of Education, Research Center for Renewable Synthetic Fuel, School of Mechanical Engineering, Shanghai Jiao Tong University, Shanghai 200240, China
2 China-UK Low Carbon College, Shanghai Jiao Tong University, Shanghai 201306, China
3 Institute of Seawater Desalination and Multipurpose Utilization of the Ministry of Natural Resources, Tianjin 300192, China

HIGHLIGHTS

- A localized high-entropy oxide (LHEO) is spatially confined within α-Fe_2O_3 to form a unique nanoarchitecture.
- The catalyst achieves low overpotential (229 mV at 10 mA/cm^2) and a small Tafel slope (34.4 mV/dec), outperforming RuO_2.
- Exceptional durability is demonstrated with stable operation over 1000 h and strong performance in seawater-based zinc-air batteries.
- LHEO-induced lattice strain and electronic modulation shift the OER pathway from AEM to LOM, lowering the energy barrier.

Keywords:
Localized high-entropy engineering
Earth-abundant oxygen evolution reaction electrocatalysts
Lattice oxygen mechanism
Seawater splitting
Zn–air battery

ABSTRACT

The development of efficient, durable, and cost-effective oxygen evolution reaction (OER) electrocatalysts is essential for advancing renewable energy technologies. Herein, a novel strategy is reported that spatially confines a nanoscale localized high-entropy oxide (LHEO) consisting of Fe, Co, Ni, Zn, and Mn within α-Fe_2O_3, forming a unique α-Fe_2O_3@LHEO nanoarchitecture. The catalyst exhibits outstanding OER performance for alkaline water splitting, achieving a current density of 10 mA/cm^2 at a low overpotential of 229 mV with a small Tafel slope of 34.4 mV/dec, significantly outperforming commercial RuO_2 (326 mV, 118.8 mV/dec). It also shows excellent long-term stability over 1000 h at 100 mA/cm^2 without notable activity degradation. Applied in rechargeable zinc–air batteries with natural seawater, the α-Fe_2O_3@LHEO cathode delivers a high power density of 88.3 mW/cm^2 and stable operation over 600 cycles, substantially surpassing the benchmark Ru-Pt electrocatalyst (74.7 mW/cm^2, 170 cycles). Combined experimental and theoretical studies reveal that LHEO induces lattice strain in α-Fe_2O_3, modulates its electronic structure, and lowers the crystal field splitting energy to stabilize high-spin Fe^{3+}. These effects enhance metallic character for efficient charge transfer and optimize the adsorption/desorption of key oxygen reaction intermediates, thus shifting the OER pathway from the conventional adsorbate evolution mechanism (AEM) to the more energetically favorable lattice oxygen mechanism (LOM) with the energy barrier reduced from 1.85 to 1.71 eV. Overall, this work proposes a novel localized high-entropy engineering approach that overcomes key bottlenecks in designing efficient and durable OER electrocatalysts based on earth-abundant materials.

© The Author(s) 2026.
This article is published with open access at link.springer.com and journal.hep.com.cn

1 Introduction

The relentless depletion of fossil fuels underscores an urgent need to transition toward a renewable energy system [1–3]. Central to this transition is the oxygen evolution reaction (OER), a fundamental process in many renewable energy technologies, including water electrolysis for green hydrogen production and metal–air

# These authors contributed equally to this work.

✉ Corresponding author. E-mail: zhoubw@sjtu.edu.cn

Article history: Received 5 February 2026, Revised 24 March 2026, Accepted 7 April 2026, Available online 30 April 2026

Special Issue: Emerging Investigators in Energy Frontier

batteries for energy storage [4–7]. However, OER is inherently hampered by sluggish kinetics, involving a complex four-electron transfer with high energy barriers ($2H_2O \rightarrow O_2 + 4H^+ + 4e^-$) [8,9]. Precious metal oxides such as IrO_2 and RuO_2 remain the benchmark OER catalysts to overcome these issues. Despite their high activity, their extreme scarcity and unaffordable price—for instance, the global iridium yield is only about 7–8 tons per year—prevent their deployment at the terawatt scales [10,11]. In this context, it is highly desirable to develop high-performance noble-metal-free OER catalysts to break the bottleneck in the renewable energy revolution [12].

Among a variety of non-precious metals, iron-based catalysts have garnered considerable interest owing to their natural abundance, low toxicity, and rich redox chemistry [13–15]. The versatile oxidation states of iron (Fe^{2+}/Fe^{3+}) support tunable electronic structures well-suited for multi-step reactions such as OER [16]. The adsorption of oxygen-containing intermediates on the catalyst surface is closely related to the spin state of the active metal [17]. Fe^{3+} exists in three distinct spin states: low-spin (LS, $t_{2g}^5\ e_g^0$), intermediate-spin (IS, $t_{2g}^4\ e_g^1$), and high-spin (HS, $t_{2g}^3\ e_g^2$) [18,19]. High-spin Fe^{3+} often plays a significant role in OER reactions [20]. On the one hand, turning the spin-electronic configuration of Fe centers to the high-spin state enables electron penetration into the antibonding π-orbitals of adsorbed species, thereby modulating intermediate adsorption strength [21,22]. On the other hand, high-spin ions can serve as spin channels, enhancing selective extraction of spin-oriented electrons and facilitating the formation of triplet oxygen molecules [23]. However, conventional iron-based catalysts suffer from inherent limitations, including poor electrical conductivity (~10^{-14} S/cm for α-Fe_2O_3), suboptimal active-site configurations, and the difficulty in stabilizing high-spin Fe^{3+} under operating conditions, all of which hinder the efficient adsorption/desorption of key reaction intermediates and impose significant energy barriers, thereby restricting overall catalytic performance [24]. Recent studies show that tailoring the local chemical environment via doping, defect engineering, and interface structuring can partially enhance catalytic properties [25–27]. Nevertheless, iron-based OER catalysts remain far from practical application.

High-entropy alloys (HEAs), composed of five or more principal elements in near-equimolar ratios, exhibit high configurational entropy and unique electronic and catalytic properties [28–30]. HEA engineering offers a promising route to improve iron-based materials by simultaneously tuning composition, strain, and defects [31–33]. Specifically, lattice distortion induced by atomic size mismatch generates abundant surface defects and oxygen vacancies, promoting OER pathway toward the lattice oxygen mechanism (LOM) [34,35]. Moreover, HEAs tune the electronic structure and d-band center of iron active sites, optimizing adsorption energies and reducing activation energy barriers [36,37]. Furthermore, the cocktail effect arising from synergistic interactions among multiple elements further enables the integration of complementary functionalities, helping to overcome the activity-stability trade-off that plagues conventional iron-based catalysts [38].

In this study, a localized high-entropy engineering strategy is proposed to improve iron-based OER performance (Fig. 1). A localized high-entropy oxide (LHEO) composed of Fe, Co, Ni, Zn, and Mn is spatially confined within α-Fe_2O_3 (α-Fe_2O_3@LHEO) for OER catalysis. During water electrolysis, α-Fe_2O_3@LHEO delivers a low overpotential of 229 mV at 10 mA/cm^2, with a distinct Tafel slope of 34.4 mV/dec in alkaline electrolyte, substantially outperforming α-Fe_2O_3 (299 mV, 61.2 mV/dec) and commercial RuO_2 (326 mV, 118.8 mV/dec). It exhibits outstanding stability for over 1000 h at 100 mA/cm^2 without significant activity degradation. When applied in a rechargeable Zn–air battery using natural seawater, a high peak power density of 88.3 mW/cm^2 and stable operation over 600 cycles are achieved, surpassing a commercial Ru-Pt catalyst (74.7 mW/cm^2, 170 cycles). Combined spectroscopic analysis and density functional theory (DFT) calculations reveal that LHEO induces lattice strain, electronic reconfiguration, and stabilization of high spin Fe^{3+} in α-Fe_2O_3. This facilitates charge transfer and optimizes intermediate adsorption energies. Meanwhile, the reaction pathway shifts from the adsorbate evolution mechanism (AEM) to the more energetically favorable LOM, with a dramatically reduced energy barrier. This study introduces a nanoscale localized high-entropy engineering strategy for developing efficient, durable, and cost-effective OER electrocatalysts based on earth-abundant materials.

2 Method

2.1 Working electrode preparation

For the three-electrode configuration, nickel foam (NF) was used as the substrate, with a LHEO/α-Fe_2O_3/carbon nanotubes (CNTs) composite catalytic layer grown *in situ* via a one-step hydrothermal route. Briefly, $Fe_2(SO_4)_3$, $ZnCl_2$, $CoCl_2$, $MnSO_4$, $NiCl_2$, and CNTs were weighed at a target molar ratio, dispersed in deionized water (DIW), and stirred until fully dissolved to form a homogeneous precursor solution, followed by ultrasonication for 30 min to ensure uniform dispersion.

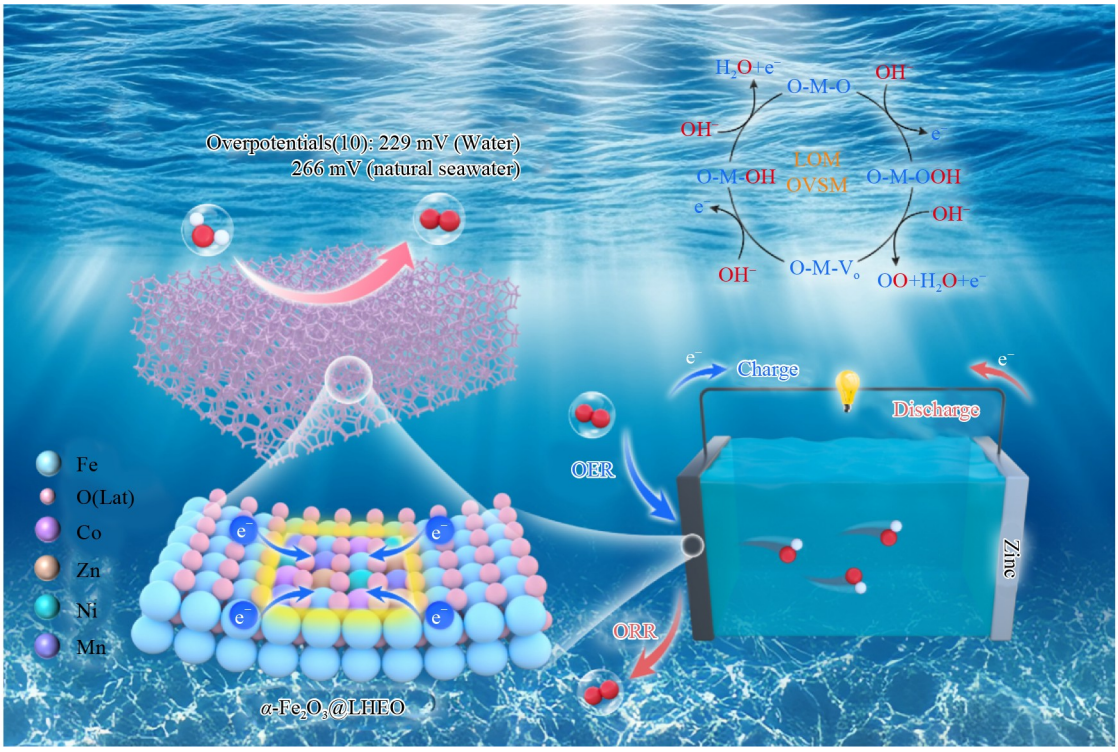

Fig. 1 Schematical illustration of the localized high-entropy engineering strategy to improve iron-based OER electrocatalysts for renewable energy technologies in water splitting and Zn–air battery (ZAB).

Commercial NF substrates (2 × 1 cm^2) were pretreated by solvent degreasing in acetone (30 min, 40 °C, ultrasonic), acid etching in 3 mol/L HCl (20 min, ultrasonic) to remove native oxides, sequential rinsing with DIW and anhydrous ethanol, and dehydration in a vacuum oven. The pretreated NF was then immersed in the precursor solution, transferred to a Teflon-lined hydrothermal autoclave, sealed, and maintained at 150 °C for 120 min to achieve *in situ* growth of the composite layer (Fig. S1). After natural cooling to ambient temperature, the NF was retrieved, and the residual solution was centrifuged to collect precipitate. Finally, the NF was rinsed alternately with DIW and ethanol to remove residual salts, air-dried at room temperature, and directly used as the working electrode for OER tests in the three-electrode system.

2.2 Pretreatment of natural seawater

Raw natural seawater was collected from the coastal area of Beihai, Guangxi Zhuang Autonomous Region, China (21.4254° N, 109.0992° E), and vacuum-filtered through Whatman Grade 1 qualitative filter paper (11 μm pore size) to remove large, suspended solids and insoluble impurities, yielding pretreated seawater.

For three-electrode electrochemical tests, the pH of 1 mol/L KOH reference solution was calibrated to 13.6 at 26 °C. Analytical grade KOH was added to pretreated seawater under stirring with real-time pH monitoring until stabilization at pH 13.6. The solution was then centrifuged at 9000 r/min (25 °C, 10 min) to remove insoluble metal hydroxides, and the supernatant was stored in a polyethylene container.

For ZAB tests, analytical grade KOH and zinc acetate dihydrate were dissolved in pretreated seawater to final concentrations of 6 and 0.2 mol/L, respectively. After 30 min of stirring, the solution was centrifuged at 10000 r/min (25 °C, 15 min), and the clear supernatant was collected as the ZAB electrolyte.

2.3 Preparation of cathode for ZAB

The ZAB cathode was fabricated on a three-layer composite substrate. Briefly, 4 mg of catalyst powder was dispersed in ethanol and ultrasonicated for 30 min to form homogeneous ink. The ink was uniformly drop-cast onto the substrate and oven-dried to obtain a catalytically active cathode.

A Zn sheet was used as the anode after sanding, ultrasonicly cleaning in ethanol, and drying. The electrolyte consisted of 6 mol/L KOH and 0.2 mol/L zinc acetate in natural seawater. The cathode, electrolyte, and anode were sequentially assembled into a rechargeable ZAB. For comparison, an IrO_2-Pt/C (1:1 mass ratio)

cathode with the same loading was prepared.

For the flexible ZAB, the same procedure was followed. A dry polyacrylic acid (PAA) gel was immersed in the electrolyte for 24 h and used as the electrolyte. A well-polished Zn foil served as the anode and was sealed in a plastic bag. After standing for 1 h, electrochemical tests were conducted.

3 Characterization

Scanning electron microscopy (SEM) images were obtained on a Quattro ESEM (FEI). Scanning transmission electron microscopy (STEM) imaging was performed on a Thermo Fisher Scientific Talos F200X S/TEM at 200 kV with a Super-energy-dispersive X-ray spectroscopy (EDS) detector. Transmission electron microscopy (TEM) images were obtained using a JEOL 2100F microscope. Electron paramagnetic resonance (EPR) spectra were recorded on a Bruker A300 instrument (Germany). X-ray diffraction (XRD) patterns were obtained using a Bruker D8 Advance diffractometer. X-ray photoelectron spectroscopy (XPS) measurements were conducted on an ESCALAB 250xi system equipped with a non-monochromatic aluminum anode, with the C 1s peak at 284.8 eV used for calibration. Inductively coupled plasma atomic emission spectroscopy (ICP-AES) measurements were conducted using an AGILENT 730 instrument. Vibrating Sample Magnetometer (VSM) were performed using MPMS-VSM at 300 K. Raman spectra were recorded on a HORIBA LabRAM HR Evolution spectrometer, which has a focal length of 800 mm and covers a spectral range from 200 to 3200 nm.

3.1 Electrochemical characterization

All electrochemical tests were performed on a CHI660E electrochemical workstation in a conventional three-electrode system with 1.0 mol/L KOH or 1.0 mol/L KOH + seawater electrolyte (pH 13.6) at 25 ± 1 °C. The working electrode was catalyst-loaded NF, the reference electrode was Hg/HgO (1 mol/L KOH), and the counter electrode was Pt mesh (99.99% purity).

All measured potentials were converted to the reversible hydrogen electrode (RHE) scale using:

$$E_{\mathrm{RHE}} = E_{\mathrm{Hg/HgO}} + 0.0591 * \mathrm{pH} + 0.098\ \mathrm{V}. \quad (1)$$

Linear sweep voltammetry (LSV) was conducted at 10 mV/s from 0.2 to 0.8 V versus RHE. iR compensation (85%) was applied. Tafel slopes were derived using

$$\eta = b\log(j) + a. \quad (2)$$

where η represents the overpotential, j is the current density, and b denotes the Tafel slope.

The electrochemical double-layer capacitances (C_{dl}) within the non-Faradaic potential region (1.024–1.224 V versus RHE) were calculated using CV curves recorded at scan rates of 20, 40, 60, 80, 100, and 120 mV/s, and the C_{dl} values were obtained by linear fitting the capacitive current differences ($\Delta_{j/2}$) versus scan rate. Electrochemical impedance spectra (EIS) of the catalyst's tests were performed at 10 mA/cm^2 over a frequency window of 10^5–0.1 Hz. Long-term catalyst durability was assessed via chronopotentiometry (CP) at various current densities.

After assembly, the ZAB was allowed to stand for 12 h. The instantaneous open-circuit potential (OCP) is measured using a multimeter and recorded. Subsequently, a CHI660E workstation was employed to conduct activity and stability tests. The OCP sampling interval was set at 60 s, and the data were monitored and recorded for 10 h. The charge–discharge curves were measured by the LSV method, with a charging range of 1.5–3.2 V, a discharging range of 1.5–0 V, and a scan rate of 10 mV/s. The power density was calculated by the product of the voltage and current of the discharge curve ($P = U \times I$). The specific capacity was determined by constant-current discharging (0.005 A) until battery failure. After recording the mass of the consumed zinc sheet, it was calculated according to $C = It/m$. For the cycle stability test, the charge and discharge currents were both set at 5 mA, with each charge and discharge step lasting 600 s. The cycling process was monitored and the data were recorded.

3.2 H_2O_2 detection

The H_2O_2 produced during anodic water oxidation was quantified via UV-Vis spectroscopy (Shimadzu UV-3600). Electrocatalytic water oxidation was run in a three-electrode setup at a fixed potential of 1.6 V vs RHE for 30 min. Post-reaction, 1 mL of 1 mol/L HCl was mixed with 3 mL of the reaction solution, then 1 mL of 0.1% OPD solution (chromogenic agent) was added. After complete mixing, the absorption spectrum of the solution was acquired from 300 to 600 nm. The characteristic 438 nm absorption peak of the OPD-H_2O_2 complex confirmed H_2O_2 production from water oxidation.

3.3 *In situ* Raman spectroscopy monitoring protocol

Electrochemical Raman spectroscopy (ERS) measurements were conducted using a conventional three-electrode setup under potentiostatic regulation. The active

working electrode was sequentially polarized at potentials ranging from the open-circuit potential (OCP) to 0.8 V versus RHE in 0.1 V increments. For every applied potential, chronoamperometric (i–t) measurements were recorded for 300 s. Raman spectra were acquired after a 5-min stabilization period to minimize transient interfacial effects. Each potential step was replicated 1–2 times to mitigate the adverse impacts of random signal fluctuations and gas bubble formation during testing.

3.4 Computational detail

DFT [39] calculations were performed using the Vienna Ab Initio Simulation Package (VASP) [40,41]. The interaction between valence electrons and ionic cores was described by the projector-augmented wave (PAW) method [42,43]. Exchange-correlation effects within the Kohn-Sham framework were treated using the Perdew-Burke-Ernzerhof (PBE) functional under the generalized gradient approximation (GGA) [44]. A plane-wave basis set with a kinetic energy cutoff of 400 eV was used to expand the wave functions. Due to the relatively large system and sampling size, only the Γ k-point is sampled in the Brillouin zone [45].

Geometry optimization was performed with convergence criteria of 0.02 eV/Å for atomic forces and 10^{-4} eV for total energy, while a stricter criterion of 10^{-6} eV was applied for precise energy calculations. During structural relaxation, the bottom two atomic layers were fixed at their bulk positions in the slab models. To avoid interactions between periodic images, a vacuum layer of at least 25 Å was introduced perpendicular to the surface for all slabs and in all three spatial dimensions for nanoclusters.

The Gibbs free energy of adsorption (ΔG) was calculated using

$$\Delta G = E_{\mathrm{ad}} + \Delta ZPE - T\Delta S, \tag{3}$$

where E_{ad} is the adsorption energy defined by

$$E_{\mathrm{ad}} = E_{\mathrm{surface+adsorbate}} - E_{\mathrm{surface}} - E_{\mathrm{adsorbate}}. \tag{4}$$

ΔZPE and ΔS are the changes in zero-point energy and entropy during adsorption [46,47].

4 Results and discussion

A LHEO composed of Fe, Co, Ni, Zn, and Mn was incorporated into α-Fe_2O_3 via a one-step hydrothermal method (see Experimental Section and Fig. S1). SEM shows that the α-Fe_2O_3@LHEO nanoarchitecture is firmly anchored on the nickel foam substrate (Fig. S2). Contact angle measurements indicate a transition from hydrophobic to hydrophilic behavior with gas-repellent properties (Fig. S3), facilitating rapid bubble release during water electrolysis.

STEM reveals α-Fe_2O_3@LHEO nanoparticles with an average size of approximately 50 nm (Fig. 2(a)). EDX mapping confirms homogeneous dispersion of the LHEO phase within α-Fe_2O_3 (Fig. 2(b)). ICP-AES indicates Fe as the main component, while the other four elements exhibit similar contents (Fig. S4). Fast Fourier transform (FFT) analysis identifies the [001] zone axis, corresponding to the exposed (001) plane of α-Fe_2O_3 (Fig. 2(c)) [48,49].

Aberration-corrected TEM (AC-TEM) further confirms the coexistence of LHEO and α-Fe_2O_3 (Figs. 2(d) and 2(e)). Notably, the LHEO region exhibits higher 3D intensity, attributed to severe lattice distortion induced by the high-entropy effect. Well-defined lattice fringes with a spacing of 0.252 nm correspond to the (110) plane of α-Fe_2O_3, while a reduced lattice spacing of 0.247 nm in the LHEO region indicates lattice contraction (Figs. 2(e) and 2(f)). EPR spectra reveal a significantly enhanced oxygen vacancy signal, evidencing that the LHEO induces substantial lattice strain and promotes oxygen vacancy formation (Fig. 2(g)).

XRD confirms that α-Fe_2O_3@LHEO retains the hematite R3c structure (α-Fe_2O_3, $a = b = 5.037$ Å, $c = 13.771$ Å, $\alpha = \beta = 90°$, $\gamma = 120°$) (JCPDS 89-0596), with no additional peaks observed (Fig. S5), indicating phase compatibility. XPS reveals a positive shift of 0.81 eV in the Fe 2p in α-Fe_2O_3@LHEO compared to pristine α-Fe_2O_3 and an increased Fe^{3+} (Figs. 2(h), S6). Additionally, the O 1s peak of pristine α-Fe_2O_3 shifts from 529.3 to 530.2 eV after LHEO incorporation (Fig. 2(i)). The presence of Co, Cr, Zn, and Mn is also confirmed (Fig. S7). These results verified successful nanoscale localization of high-entropy oxide in α-Fe_2O_3, and strong electronic interactions with α-Fe_2O_3.

DFT calculations were conducted to study the structural and electronic properties of the electrocatalysts. The introduction of LHEO induces lattice distortion in α-Fe_2O_3, as reflected by a reduced average Fe–O bond length (1.91 Å in α-Fe_2O_3@LHEO versus 1.93 Å in pristine α-Fe_2O_3; Fig. 3(a)). Charge density difference and Bader charge analysis (Fig. 3(b) and Table S1) reveal electron transfer from α-Fe_2O_3 to LHEO, lowering the average Bader charge on both Fe and O sites in α-Fe_2O_3@LHEO. This charge redistribution signifies an increased oxidation state of Fe, which is corroborated by the electronic density of states (DOS). The total DOS shows an elevated number of occupied states near the Fermi level in α-Fe_2O_3@LHEO, indicating enhanced electrical conductivity, which is conducive to rapid electron transfer during electrocatalysis (Fig. S8).

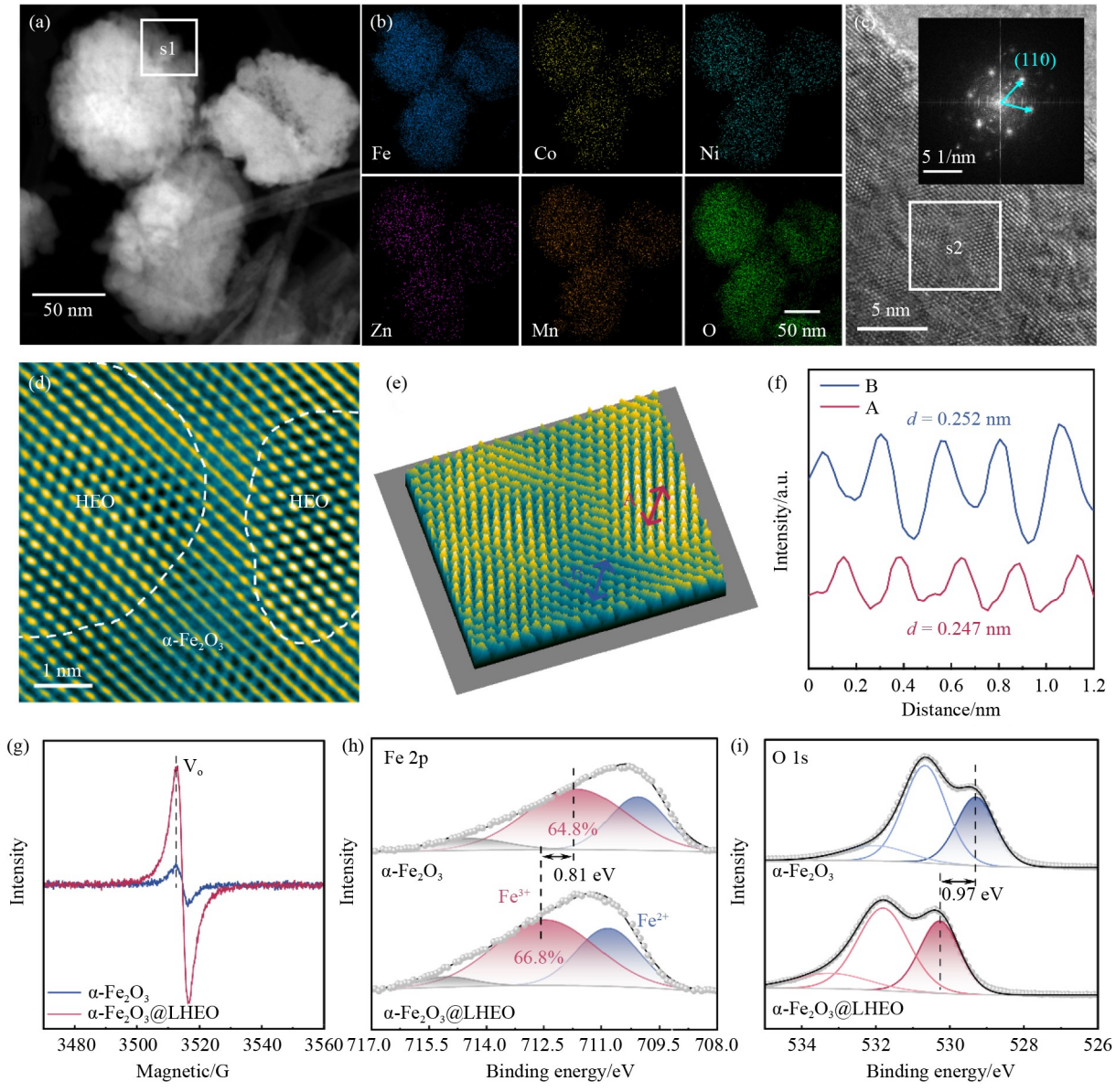

Fig. 2 Synthesis and characterization of α-Fe_2O_3@LHEO.

(a) STEM; (b) EDS elemental mapping images of α-Fe_2O_3@LHEO; (c) AC-TEM image of α-Fe_2O_3@LHEO and the corresponding FFT transformation; (d) high-resolution AC-TEM image of α-Fe_2O_3@LHEO; (e) 3D surface intensity; (f) atom intensity line in (e); (g) EPR patterns of α-Fe_2O_3@LHEO and α-Fe_2O_3, (h) high-resolution XPS spectra of Fe 2p; (i) high-resolution XPS spectra of O 1s in α-Fe_2O_3@LHEO and α-Fe_2O_3.

More critically, projection of the DOS onto the Fe-3d orbitals reveals a downshift of the Fe d-band center from −1.51 eV in pristine α-Fe_2O_3 to −1.63 eV in α-Fe_2O_3@LHEO (Fig. 3(c)). This shift results from increased nuclear attraction upon electron loss, which contracts the d orbitals. This lowered d-band center is favorable for weakening the adsorption strength of oxygenated intermediates on the catalyst surface. It thereby lowers the energy barrier of the potential-determining step in the OER, as further discussed below.

Crystal field theory provides additional insight into this electronic regulation. The crystal field splitting energy (Δ_0) decreases significantly from Δ_0 = 0.106 eV in α-Fe_2O_3 to 0.087 eV in α-Fe_2O_3@LHEO (Figs. 3(d), S9). A smaller Δ_0 favors a high-spin state of Fe^{3+} ions (Fig. 3(e)) by promoting electron occupation of higher-energy orbitals rather than spin pairing [50]. This is supported by room-temperature magnetic hysteresis (M-H) loop combined with EPR results (Figs. 2(g), S10) [51–53]. This high-spin state results in a larger ionic radius of

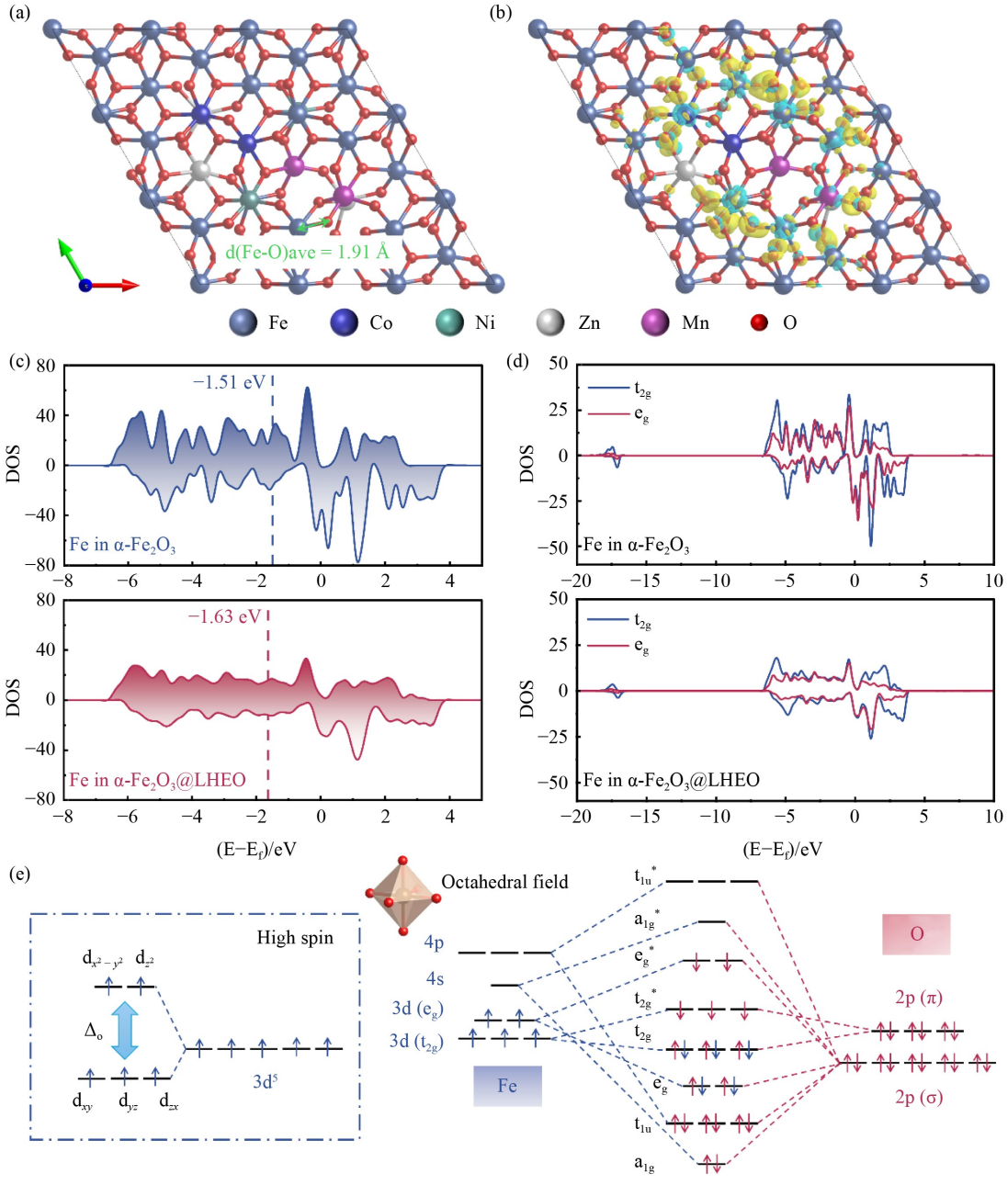

Fig. 3 Theoretical investigations of the electronic/molecular structure of α-Fe_2O_3@LHEO.

(a) Optimized structures; (b) charge density of α-Fe_2O_3@LHEO (yellow representing electron accumulation, blue represents electron depletion); (c) PDOS profile on Fe orbitals of α-Fe_2O_3@LHEO and pure α-Fe_2O_3; (d) PDOS on the spin orbitals of t_{2g} and e_g of Fe atoms; (e) crystal field and electronic structure of FeO_6 with high-spin Fe^{3+}.

Fe^{3+}, providing a fundamental explanation for the observed lattice contraction [54–56].

Overall, localized high-entropy engineering not only downshifts the Fe d-band center to optimize intermediate adsorption but also introduces defects that significantly enhance the intrinsic conductivity of the material, thereby synergistically contributing to the exceptional OER catalytic performance, as discussed below.

4.1 Electrocatalytic water splitting performance of α-Fe_2O_3@LHEO

The OER performance of water electrolysis over α-Fe_2O_3@LHEO was first evaluated in 1.0 mol/L KOH aqueous solution using a standard three-electrode configuration (Figs. S11 and S12). The iR-corrected LSV curves were collected at a scan rate of 10 mV/s. As shown in

Fig. 4(a), the overpotential (η) of α-Fe_2O_3@LHEO is markedly lower than that of commercial RuO_2. Specifically, the overpotentials of α-Fe_2O_3@LHEO at current densities of 10 and 100 mA/cm^2 were measured to be 229 and 306 mV, respectively. Meanwhile, the corresponding Tafel slope of α-Fe_2O_3@LHEO is as low as 34.4 mV/dec, substantially lower than that of RuO_2 (118.8 mV/dec), indicating accelerated OER kinetics (Fig. 4(b)).

To elucidate the origin of the exceptional performance, the electrochemical active surface area (ECSA) was determined via C_{dl} measurements in the non-Faradaic region (1.024–1.224 V versus RHE; Fig. S13). The C_{dl} of α-Fe_2O_3@LHEO is 6.8 mF/cm^2, significantly higher than those of α-Fe_2O_3 (4.7 mF/cm^2) and RuO_2 (4.2 mF/cm^2) (Fig. 4(c)), corresponding to an ECSA of 85 cm^2 (Table S2). This large active area provides abundant reaction sites for catalysis. Furthermore, ECSA-normalized polarization curves (Fig. S14) show that, at a given overpotential, the current density of α-Fe_2O_3@LHEO is significantly higher than that of α-Fe_2O_3. This result confirms that the enhanced catalytic performance of α-Fe_2O_3@LHEO arises not only from increased active sites but also from enhanced intrinsic activity per site. EIS measurements reveal a lower charge-transfer resistance for α-Fe_2O_3@LHEO compared to α-Fe_2O_3 and RuO_2 (Fig. 4(d)). This finding is in excellent agreement with the DFT results above, suggesting facilitated charge

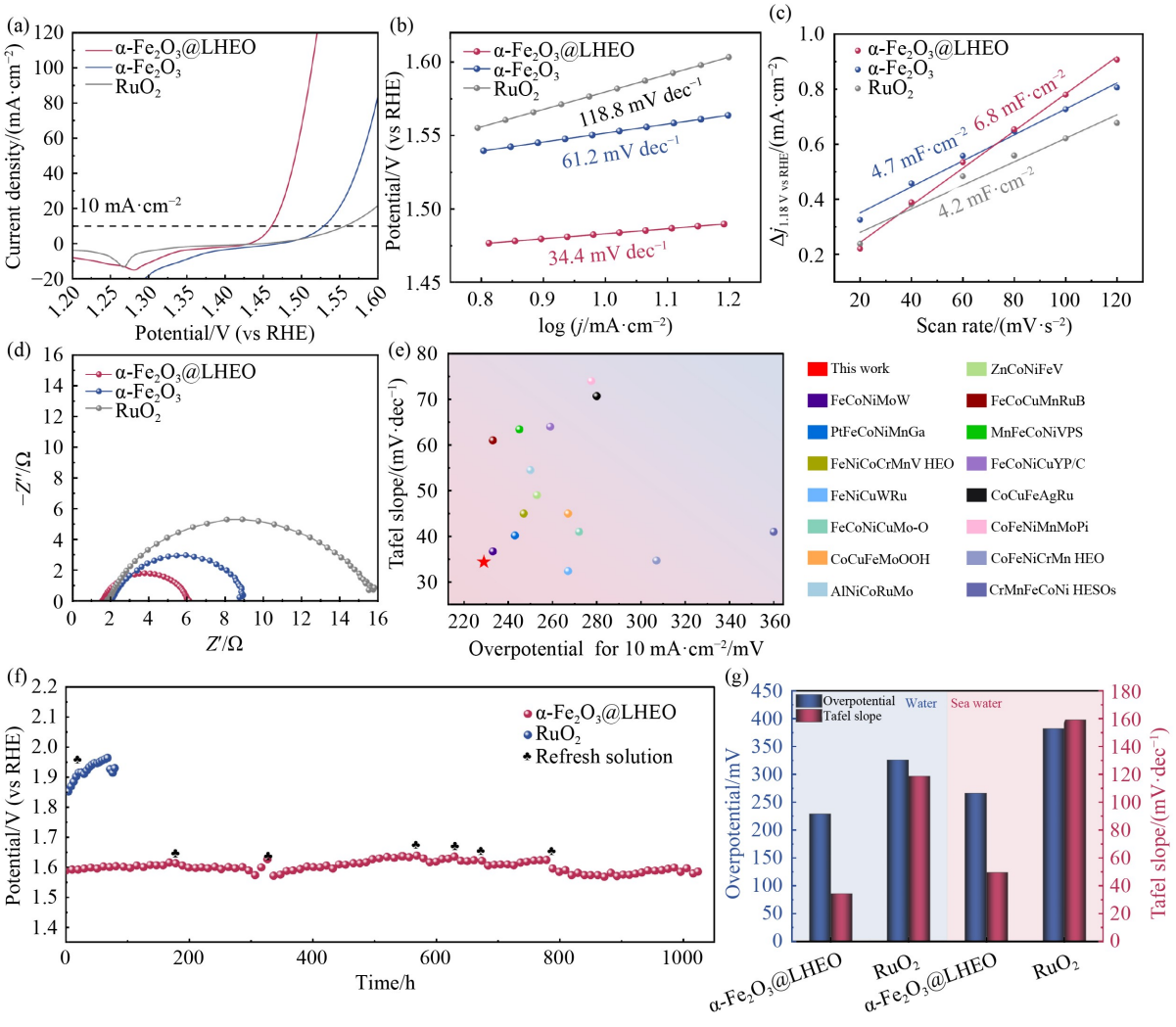

Fig. 4 OER performance in alkaline electrolyte for water/seawater electrolysis.

(a) LSV curves of α-Fe_2O_3@LHEO, α-Fe_2O_3, and commercial RuO_2; (b) Tafel slopes of different OER catalysts measured at a scan rate of 10 mV/s; (c) capacitive current density as a function of the scan rate; (d) EIS measurements for α-Fe_2O_3, α-Fe_2O_3@LHEO, and RuO_2; (e) summary of high entropy catalysts for OER in alkaline water; (f) *v*–*t* curves at the current densities of 100 mA/cm^2; (g) performance summary of different electrocatalysts at 10 mA/cm^2.

transfer upon the introduction of LHEO.

Compared with recently reported high-entropy OER electrocatalysts, the alkaline OER catalyst presented in this work demonstrates superior performance (Fig. 4(e) and Table S3). Notably, α-Fe_2O_3@LHEO suppresses the formation of H_2O_2 compared to α-Fe_2O_3, as revealed by UV-Vis spectroscopy (Fig. S15 and S16). In addition, α-Fe_2O_3@LHEO exhibits excellent stability, maintaining operation for nearly 1000 h at a high current density of 100 mA/cm^2, highlighting its potential for storing renewable electricity as green H_2 without noble metals (Fig. 4(f)). After the stability test, no collapse of the NF framework or detachment of α-Fe_2O_3@LHEO was observed (Figs. S17–S19).

To broaden its applicability, the catalyst was also evaluated for OER in natural seawater electrolyte (Fig. S20 and Table S4). As illustrated in Figs. 4(g) and S21, α-Fe_2O_3@LHEO maintains a substantial overpotential advantage over RuO_2 and exhibits faster OER kinetics in natural seawater, as reflected by a lower Tafel slope (49.5 mV/dec; Fig. S22). The measured C_{dl} value of α-Fe_2O_3@LHEO (5.2 mF/cm^2) is 1.79 times that of RuO_2 (2.9 mF/cm^2) (Figs. S23 and S24). Meanwhile, α-Fe_2O_3@LHEO shows more efficient charge transfer in seawater (Fig. S25). These results demonstrate that localized high-entropy oxides in α-Fe_2O_3 serve as a promising alternative to noble metals as efficient and stable OER electrocatalysts for both water and seawater electrolysis.

To further investigate the origin of the exceptional catalytic performance, the pH-dependent OER activity was measured (Fig. 5(a)) [57]. The significantly stronger

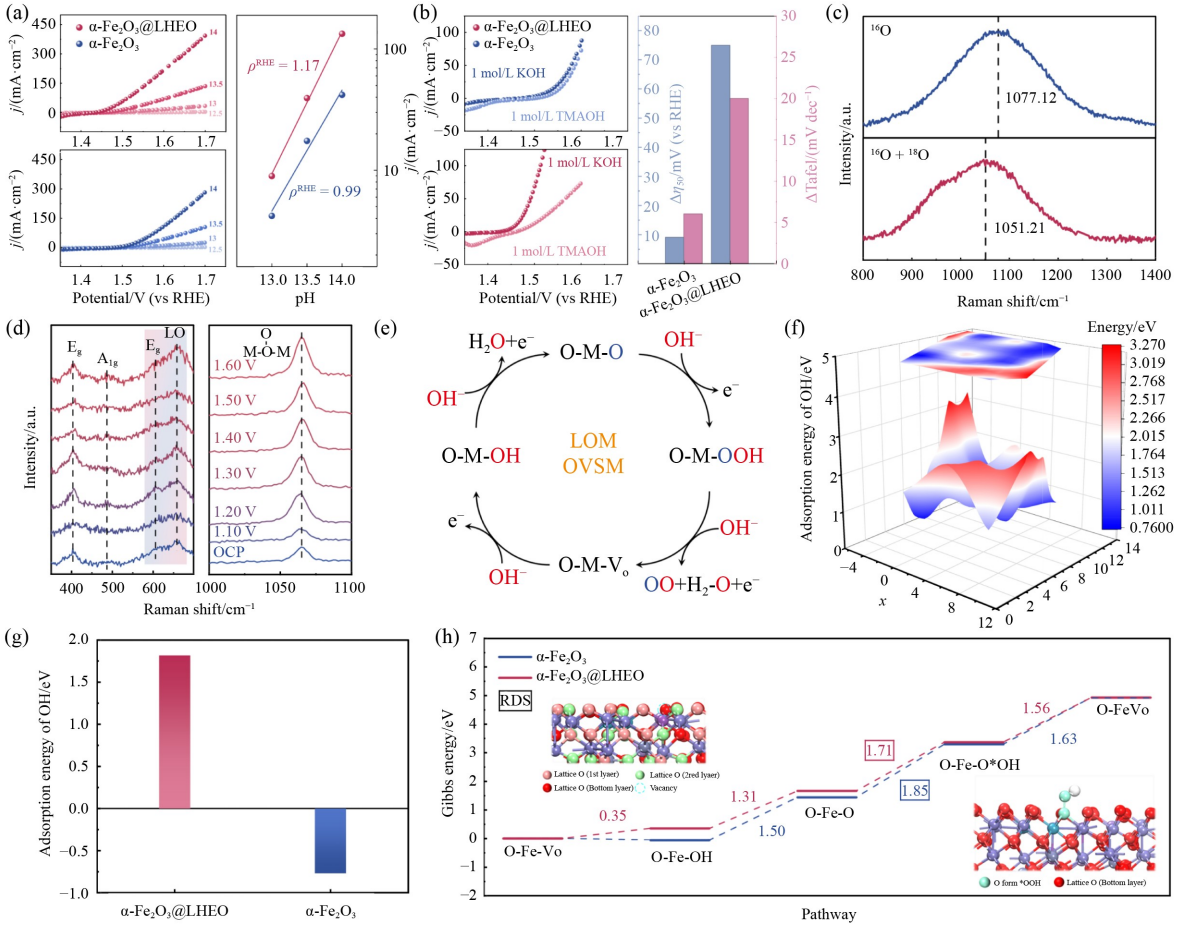

Fig. 5 OER mechanism investigation.

(a) pH-dependent OER performance of α-Fe_2O_3@LHEO and α-Fe_2O_3; (b) OER test using TMAOH as molecular probe over α-Fe_2O_3@LHEO and α-Fe_2O_3; (c) *in situ* Raman spectroscopic characterizations under applied potential over α-Fe_2O_3@LHEO with and without $H_2{}^{18}O$; (d) *in situ* Raman spectra of α-Fe_2O_3@LHEO under different applied potentials; (e) schematic illustration of the LOM pathway; (f) calculated potential energy surface for *OH adsorption on metal sites of α-Fe_2O_3@LHEO; (g) comparison of *OH adsorption energies on metal sites for α-Fe_2O_3@LHEO and α-Fe_2O_3; (h) Gibbs free energy diagram of the OER pathway over α-Fe_2O_3@LHEO and α-Fe_2O_3.

pH dependence of the OER rate (higher j versus pH slope) for α-Fe_2O_3@LHEO is consistent with the proton-electron non-concerted transfer feature of the LOM pathway, which is distinctly different from the AEM behavior of pristine α-Fe_2O_3. The OER performance of α-Fe_2O_3@LHEO was further tested in 1 mol/L TMAOH (Fig. S26), showing significantly reduced OER activity and slower kinetics compared to those in 1 mol/L KOH (Fig. 5(b)) [58]. This is attributed to TMA^+ consuming surface O_2^{2-}/O^{2-} active species, thereby suppressing the LOM-OER process. These results confirm that the reaction pathway shifts from AEM to LOM upon the introduction of localized high-entropy oxides in α-Fe_2O_3.

Surface Raman spectroscopy (SRS) characterization was performed to gain deeper insight into the reaction mechanism using ^{18}O-labeled H_2O. As illustrated in Fig. 5(c), the characteristic peak at 1050–1100 cm^{-1} is assigned to the metal-oxygen (M–O) stretching vibration. Notably, this peak in the isotopically labeled $H_2{}^{18}O$ electrolyte exhibits a negative shift from 1077.12 to 1051.21 cm^{-1} compared to H_2O. This shift is attributed to the substitution of lattice M–^{16}O with M–^{18}O [59]. These observations provide strong evidence that the LOM dominates OER catalysis over α-Fe_2O_3@LHEO.

Further investigation was performed using *in situ* Raman spectroscopy under varying applied potentials (Fig. 5(d)). In the transverse optical (TO) region, one spectral peak at ~490 cm^{-1} is assigned to the symmetric A_{1g} mode, while two additional peaks at ~410 and ~610 cm^{-1} correspond to doubly degenerate E_g modes. An additional peak at 660 cm^{-1} is observed, which can be ascribed to the relaxation of longitudinal optical (LO) phonon selection rules induced by oxygen vacancies [60]. The intensity ratio of the LO mode to the E_g mode (I[LO]/I[E_g]) was employed to quantify variation in oxygen vacancy content [61]. As illustrated in Fig. S27, the oxygen vacancy concentration exhibits a fluctuating upward trend with increasing applied potential, indicating a dynamic generation-consumption cycle during the OER. Additionally, the peak located at ~1070 cm^{-1} is assigned to bridging peroxide species (M–O_2–M), whose intensity increases progressively with increasing applied potential. Combined with the EPR results (Fig. 2(g)), these findings indicate that the reaction pathway shifts from AEM in α-Fe_2O_3 to LOM in α-Fe_2O_3@LHEO (Fig. 5(e)).

DFT calculations were further conducted to elucidate the reaction mechanism at the atomic scale. Since the characteristic step of AEM involves OH adsorption on metal sites, a potential energy surface based on OH adsorption free energies was constructed for α-Fe_2O_3@LHEO (Figs. 5(f) and S28). As shown in Fig. 5(g), OH adsorption on pristine α-Fe_2O_3 exhibits negative adsorption energy, indicating that the formation of Fe-OH intermediates is energetically favorable in the absence of LHEO. This further supports the role of LHEO in shifting the mechanism from AEM to LOM.

The OER pathways over α-Fe_2O_3@LHEO and α-Fe_2O_3 were further calculated (Figs. 5(h), S29 and S30). The reaction initiates at abundant surface oxygen vacancies, where a solution-phase OH^- fills an oxygen vacancy and undergoes deprotonation. Subsequently, OH is adsorbed onto a lattice oxygen site to form a Fe-OOH intermediate, followed by deprotonation of OOH and regeneration of oxygen vacancy. The OOH deprotonation step (O-Fe-OOH + OH^- → O-Fe-OO + H_2O + e^-) is identified as the rate-determining step (RDS). Notably, the introduction of LHEO lowers the energy barrier of the RDS from 1.85 to 1.71 eV.

4.2 Rechargeable ZAB

To broaden the application, α-Fe_2O_3@LHEO was employed as the air electrode (catalyst loading: 0.25 mg/cm^2) in a rechargeable ZAB, with commercial Pt/C serving as the cathode (Fig. S31). The battery was assembled in a layered configuration (Fig. S32) and tested in a 6 mol/L KOH-natural seawater electrolyte containing 0.20 mol/L $Zn(Ac)_2$, using a 0.3 mm thick zinc plate as the anode. The α-Fe_2O_3@LHEO + Pt/C based ZAB achieved an open-circuit potential of 1.415 V, surpassing that of RuO_2 + Pt/C (1.349 V) (Fig. 6(a)). As shown in Fig. 6(b), it also delivered a higher peak power density of 88.3 mW/cm^2, compared to 74.7 mW/cm^2 for the RuO_2 + Pt/C counterpart. At a current density of 5 mA/cm^2, the specific discharge capacity of α-Fe_2O_3@LHEO + Pt/C reached 819.9 mAh/g_{Zn} (Figs. 6(c) and S33), exceeding the 790.9 mAh/g_{Zn} obtained with RuO_2 + Pt/C. Long-time cycling tests at 5 mA/cm^2 further confirmed the superior stability of the α-Fe_2O_3@LHEO + Pt/C system (Figs. 6(d) and 6(e)).

It exhibited initial charge/discharge voltages of 2.08 V and 1.14 V, respectively, yielding a voltage gap (ΔE) of 0.93 V, and a corresponding round-trip efficiency of 54.8%. After 600 cycles, the voltage gap increased by only 1.07 mV. In contrast, the RuO_2 + Pt/C battery, although showing a slightly higher initial efficiency of 56.7% (charge: 2.06 V, discharge: 1.17 V), suffered from rapid degradation, with the voltage gap widening to 1.30 V after only 170 cycles. These results highlight the markedly improved energy conversion efficiency and cycling durability of the α-Fe_2O_3@LHEO-based electrode.

Given the growing promise of all-solid-state ZAB as efficient and sustainable power sources, a flexible all-solid-state ZAB (F-ZAB) was further fabricated. The

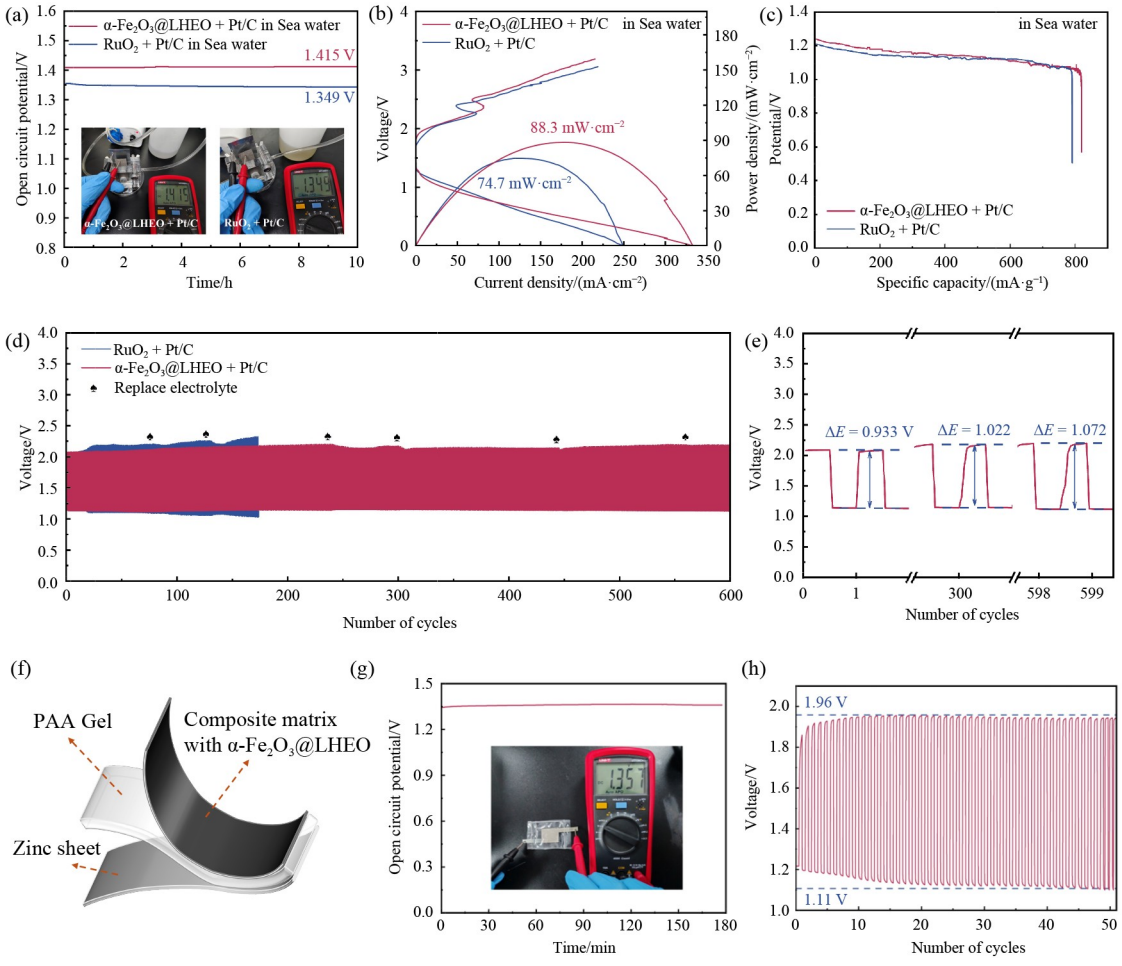

Fig. 6 Rechargeable ZAB performance in natural seawater.

(a) Open circuit voltage curves for 10 h and digital photos of α-Fe_2O_3@LHEO + Pt/C and RuO_2 + Pt/C based Zn–air batteries; (b) polarization curves of α-Fe_2O_3@LHEO + Pt/C and RuO_2 + Pt/C, and their corresponding power density curves; (c) specific discharge capacity of α-Fe_2O_3@LHEO + Pt/C and RuO_2 + Pt/C at a current density of 5 mA/cm^2; (d, e) charge–discharge cycle curves; (f) schematic illustration of the flexible rechargeable ZAB with α-Fe_2O_3@LHEO + Pt/C couple as the air cathode electrocatalyst; (g) open circuit voltage curves for 180 min and digital photo of α-Fe_2O_3@LHEO + Pt/C based F-ZAB to show open-circuit potential; (h) charge-discharge cycle.

device consists of a nickel-foam-supported α-Fe_2O_3@LHEO + Pt/C integrated electrode as the air cathode, a natural-seawater-soaked alkaline polyacrylic acid (PAA) gel as the electrolyte, and a Zn foil as the anode (Fig. 6(f)). The assembled F-ZAB achieved an open-circuit voltage of 1.36 V (Fig. 6(g)) and delivered a high power density of 36.4 mW/cm^2 (Fig. S34). During galvanostatic cycling at 5.0 mA/cm^2, it exhibited stable charge and discharge voltages of 1.96 and 1.11 V, respectively (Fig. 6(h)). The resulting ΔE of 0.85 V corresponds to a round-trip efficiency of 56.6%, and the battery maintained stable operation for over 50 cycles. The flexibility of the device was also validated, as it retained a consistent open-circuit voltage of ~1.32 V under bending angles of 120°, 90°, and 60° (Fig. S35). Compared to conventional liquid-electrolyte ZABs, this rechargeable all-solid-state design offers distinct advantages, including compact design, mechanical flexibility, high power density, and improved operational safety.

5 Conclusions

This work develops a novel localized high-entropy engineering strategy to construct a high-performance α-Fe_2O_3@LHEO electrocatalyst via spatially confining nanoscale Fe-Co-Ni-Zn-Mn high-entropy oxide within the α-Fe_2O_3 lattice. This unique design breaks the intrinsic bottlenecks of conventional iron-based OER electrocatalysts at the electronic and atomic levels,

delivering exceptional alkaline OER activity with greatly accelerated reaction kinetics, ultra-long operational stability under high current density, and outstanding performance in natural seawater-based rechargeable Zn-air batteries, far outperforming commercial noble metal benchmark catalysts.

Combined experimental characterizations and theoretical calculations reveal that the core of this performance breakthrough lies in the localized high-entropy effect: it induces lattice strain in α-Fe_2O_3, tailors the electronic structure, and reduces the crystal field splitting energy to stabilize high-spin Fe^{3+}. These synergistic effects not only enhance charge transfer efficiency and optimize the adsorption/desorption of key oxygenated intermediates, but also switch the OER pathway from the conventional AEM to the more energetically favorable LOM, with the rate-determining step energy barrier reduced from 1.85 to 1.71 eV.

More importantly, the nanoscale localized high-entropy engineering proposed in this work breaks through the limitations of traditional bulk high-entropy material design and single modification strategies, establishing a new paradigm for the rational design of efficient and durable OER electrocatalysts using earth-abundant elements.

Acknowledgements This work was supported by the Shanghai Municipal Science and Technology Major Project, Shanghai Pilot Program for Basic Research-Shanghai Jiao Tong University (Grant No. 21T11400211), the National Natural Science Foundation of China (Grant No. 22579110), the Science and Technology Program of Tianjin (Grant Nos. 24YFZCSN00080 and 25ZYCGYS00020), the special basic research fund for central public welfare institute of China (Grant No. K-JBYWF-2024-QR-09) and the Doctoral Student Program of the Young S&T Talents Cultivation Project (CAST).

Competing Interests Zhen Huang is the Editor-in-Chief of *ENGINEERING Energy*, who was excluded from the peer-review process and all editorial decisions related to the acceptance and publication of this article. Peer-review was handled independently by the other editors to minimise bias.

Electronic Supplementary Material Supplementary material is available in the online version of this article at https://doi.org/10.1007/s11708-026-1067-z and is accessible for authorized users.

Open Access This article is licensed under a Creative Commons Attribution 4.0 International License, which permits use, sharing, adaptation, distribution and reproduction in any medium or format, as long as you give appropriate credit to the original author(s) and the source, provide a link to the Creative Commons license, and indicate if changes were made. The images or other third party material in this article are included in the article's Creative Commons license, unless indicated otherwise in a credit line to the material. If material is not included in the article's Creative Commons license and your intended use is not permitted by statutory regulation or exceeds the permitted use, you will need to obtain permission directly from the copyright holder. To view a copy of this license, visit http://creativecommons.org/licenses/by/4.0/

References

1. Mondal S, Das R C, Du Y, et al. Flexocatalytic hydrogen generation and organics degradation by nano $SrTiO_3$. Advanced Science, 2025, 12(23): 2500034
2. Chu S, Wang Q. Climate change and innovative paths to a more sustainable future. Frontiers in Energy, 2024, 18(6): 717–726
3. Miao D, Li J, Ren J, et al. Exploring the potential of Ni-based hydrogen evolution catalysts in anion exchange membrane water electrolyzer. Advanced Materials, 2026, 38(10): e20491
4. Li Y, Qiu L, Tian R, et al. Chirality engineering of nanostructured copper oxide for enhancing oxygen evolution from water electrolysis. Small, 2024, 20(52): 2408248
5. Tian R, Huang L, Li Y, et al. Spin-blockade effect of chiral multi-branch Au nanoparticles for mediating oxygen evolution reaction of electro-catalytic water splitting. Chemical Engineering Journal, 2025, 520: 165517
6. Huang L, Wang T, Li Y, et al. Chiral helically grooved gold nanoarrows for concurrently enhancing oxygen and hydrogen evolution from electrochemical water splitting. Science China Chemistry, 2024, 67(11): 3767–3776
7. Li J, Miao D, Guo X, et al. Sustainable zinc–air batteries: Innovations, challenges, and pathways to commercialization. Small, 2025, 21(49): e08482
8. Chen D, Yu R, Yu K, et al. Bicontinuous RuO_2 nanoreactors for acidic water oxidation. Nature Communications, 2024, 15(1): 3928
9. Sha Q, Wang S, Yan L, et al. 10000-h-stable intermittent alkaline seawater electrolysis. Nature, 2025, 639(8054): 360–367
10. Wang X, Xu L, Li C, et al. Developing a class of dual atom materials for multifunctional catalytic reactions. Nature Communications, 2023, 14(1): 7210
11. Hong Q L, Xiao X, Ai X, et al. Organic interface enhanced electrocatalysis. Chemical Society Reviews, 2025, 54(21): 9849–9875
12. Feng W, Chang B, Ren Y, et al. Proton exchange membrane water splitting: Advances in electrode structure and mass-charge transport optimization. Advanced Materials, 2025, 37(15): 2416012
13. Song W, Xia C, Zaman S, et al. Advances in stability of NiFe-based anodes toward oxygen evolution reaction for alkaline water electrolysis. Small, 2024, 20(48): 2406075
14. Li Y, Talib S H, Liu D, et al. Improved oxygen evolution reaction performance in $Co_{0.4}Mn_{0.6}O_2$ nanosheets through Triple-doping (Cu, P, N) strategy and its application to Zn–air battery. Applied Catalysis B: Environmental, 2023, 320: 122023
15. Niu H J, Ran N, Zhou W, et al. Synergistic atomic environment optimization of nickel–iron dual sites by Co doping and Cr vacancy for electrocatalytic oxygen evolution. Journal of the American Chemical Society, 2025, 147(3): 2607–2615
16. Chen H, Liu Y, Zhang H, et al. Resolving the valence of iron oxides by resonant photoemission spectroscopy. Journal of Physical Chemistry Letters, 2025, 16(42): 10975–10981

17. Lou S, Wen G, Xu S, et al. Stabilizing the high spin cobalt atoms by local magnetic asymmetry in p-block metals-doped spinel $MnCo_2O_4$ catalysts for efficient oxygen reduction. Advanced Materials, 2026, 38(2): e13681
18. Wang Y, Meng P, Yang Z, et al. Regulation of atomic Fe-spin state by crystal field and magnetic field for enhanced oxygen electrocatalysis in rechargeable zinc–air batteries. Angewandte Chemie International Edition, 2023, 62(28): e202304229
19. Li Y, Sun H, Ren L, et al. Asymmetric coordination regulating D-orbital spin-electron filling in single-atom iron catalyst for efficient oxygen reduction. Angewandte Chemie International Edition, 2024, 63(28): e202405334
20. Wang X T, Ouyang T, Wang L, et al. Redox-inert Fe^{3+} ions in octahedral sites of Co–Fe spinel oxides with enhanced oxygen catalytic activity for rechargeable zinc–air batteries. Angewandte Chemie International Edition, 2019, 58(38): 13291–13296
21. Ouyang T, Wang X T, Mai X Q, et al. Coupling magnetic single-crystal $Co_2Mo_3O_8$ with ultrathin nitrogen-rich carbon layer for oxygen evolution reaction. Angewandte Chemie International Edition, 2020, 59(29): 11948–11957
22. Yang G, Zhu J, Yuan P, et al. Regulating Fe-spin state by atomically dispersed Mn–N in Fe–N–C catalysts with high oxygen reduction activity. Nature Communications, 2021, 12(1): 1734
23. Sun Y, Sun S, Yang H, et al. Spin-related electron transfer and orbital interactions in oxygen electrocatalysis. Advanced Materials, 2020, 32(39): 2003297
24. Ma S, Zhu Q, Zheng Z, et al. Nanosized $LiNi_{1-x}Fe_xPO_4$ embedded in a mesoporous carbon matrix for high-performance electrochemical water splitting. Chemical Communications (Cambridge), 2015, 51(87): 15815–15818
25. Dong H, Luo L, Zhou S, et al. Spin magnetic effect activate dual site intramolecular O—O bridging for nickel-iron hydroxide enhanced oxygen evolution catalysis. Advanced Science, 2025, 12(10): 2415525
26. Li N, Hadt R G, Hayes D, et al. Detection of high-valent iron species in alloyed oxidic cobaltates for catalysing the oxygen evolution reaction. Nature Communications, 2021, 12(1): 4218
27. Guerra Demingos P, Chen Z, Ni X, et al. Computational engineering of Non-van der Waals 2D magnetene for enhanced oxygen evolution and reduction reactions. ChemSusChem, 2025, 18(3): e202401157
28. Sun L, Wen K, Li G, et al. High-entropy alloys in catalysis: Progress, challenges, and prospects. ACS Materials Au, 2024, 4(6): 547–556
29. Yao Y, Dong Q, Brozena A, et al. High-entropy nanoparticles: Synthesis–structure–property relationships and data-driven discovery. Science, 2022, 376(6589): eabn3103
30. Ren J T, Chen L, Wang H Y, et al. High-entropy alloys in electrocatalysis: From fundamentals to applications. Chemical Society Reviews, 2023, 52(23): 8319–8373
31. Chida Y, Tomimori T, Ebata T, et al. Experimental study platform for electrocatalysis of atomic-level controlled high-entropy alloy surfaces. Nature Communications, 2023, 14(1): 4492
32. Wan Y, Wei W, Ding S, et al. A Multi-site synergistic effect in high-entropy alloy for efficient hydrogen evolution. Advanced Functional Materials, 2025, 35(5): 2414554
33. Ma Y, Ma Y, Wang Q, et al. High-entropy energy materials: challenges and new opportunities. Energy & Environmental Science, 2021, 14(5): 2883–2905
34. Zhao X, Cheng H, Wu L, et al. Sub-angstrom strain in high-entropy intermetallic boosts the oxygen reduction reaction in fuel cell cathodes. Nature Communications, 2025, 16(1): 7547
35. Zhang L, Zeng Y, Li H, et al. Engineering B-site configurational entropy in perovskite oxides for enhanced alkaline oxygen evolution reaction. ChemSusChem, 2026, 19(3): e70498
36. Xu Z, Wang Y, Zheng Z, et al. Electrochemical degradation of plastic waste coupled with hydrogen evolution in seawater using Rosette-like high-entropy oxides. Advanced Science, 2025, 12(35): e07023
37. Zhao Y, Wu J, Cao X, et al. High-entropy materials for water splitting: An atomic nanoengineering approach to sustainable hydrogen production. Advanced Materials, 2025, 37(36): 2506117
38. Chen J, Ma J, Huang T, et al. Iridium-free high-entropy alloy for acidic water oxidation at high current densities. Angewandte Chemie International Edition, 2025, 64(21): e202503330
39. Kohn W, Sham L J. Self-consistent equations including exchange and correlationeffects. Physical Review, 1965, 140(4A): A1133–A1138
40. Kresse G, Furthmüller J. Efficient iterative schemes for ab initio total-energy calculations using a plane-wave basis set. Physical Review B: Condensed Matter, 1996, 54(16): 11169–11186
41. Kresse G, Joubert D. From ultrasoft pseudopotentials to the projector augmented-wave method. Physical Review B: Condensed Matter, 1999, 59(3): 1758–1775
42. Perdew J P, Chevary J A, Vosko S H, et al. Atoms, molecules, solids, and surfaces: Applications of the generalized gradient approximation for exchange and correlation. Physical Review B: Condensed Matter, 1992, 46(11): 6671–6687
43. Blöchl P E. Projector augmented-wave method. Physical Review B: Condensed Matter, 1994, 50(24): 17953–17979
44. Perdew J P, Burke K, Ernzerhof M. Generalized gradient approximation made simple. Physical Review Letters, 1996, 77(18): 3865–3868
45. Monkhorst H J, Pack J D. Special points for Brillouin-zone integrations. Physical Review. B, Solid State, 1976, 13(12): 5188–5192
46. Nørskov J K, Rossmeisl J, Logadottir A, et al. Origin of the overpotential for oxygen reduction at a fuel-cell cathode. Journal of Physical Chemistry B, 2004, 108(46): 17886–17892
47. Wang V, Xu N, Liu J C, et al. VASPKIT: A user-friendly interface facilitating high-throughput computing and analysis using VASP code. Computer Physics Communications, 2021, 267: 108033
48. Jia C J, Sun L D, Yan Z G, et al. Single-crystalline iron oxide nanotubes. Angewandte Chemie International Edition, 2005,

44(28): 4328–4333
49. Huang H, Wang J, Liu Y, et al. Stacking textured films on lattice-mismatched transparent conducting oxides via matched Voronoi cell of oxygen sublattice. Nature Materials, 2024, 23(3): 383–390
50. Li C F, Xie L J, Zhao J W, et al. Interfacial electronic modulation by Fe_2O_3/NiFe-LDHs heterostructures for efficient oxygen evolution at high current density. Applied Catalysis B: Environmental, 2022, 306: 121097
51. Gao H, Shang L, Qian S, et al. Precise axial coordination tailors the spin state of single-atom iron for boosted oxygen reduction electrocatalysis. Advanced Functional Materials, 2026， early access, https://doi.org/10.1002/adfm.202531932
52. Zhou Z, Li B, Li J, et al. Strain-induced magnetic ordering unlocks spin-conserved catalysis in lithium-oxygen batteries. Advanced Materials, 2026, 72632(17): e72632
53. Lv Y, Fang Z, Zhou L, et al. Beyond volcano top of transition metal-based electrocatalysts triggered by spin state modulation. Advanced Functional Materials, 2026, 36(19): e20395
54. Shen G, Pan L, Zhang R, et al. Low-spin-state hematite with superior adsorption of anionic contaminations for water purification. Advanced Materials, 2020, 32(11): 1905988
55. Jiang J, Sun F, Zhou S, et al. Atomic-level insight into super-efficient electrocatalytic oxygen evolution on iron and vanadium co-doped nickel (oxy)hydroxide. Nature Communications, 2018, 9(1): 2885
56. Suntivich J, Gasteiger H A, Yabuuchi N, et al. Design principles for oxygen-reduction activity on perovskite oxide catalysts for fuel cells and metal–air batteries. Nature Chemistry, 2011, 3(7): 546–550
57. Yao T, Fu Q, Wang K, et al. Decoupling the effects of ruthenium sites and oxygen vacancies on the mechanism regulation of acidic water oxidation. ACS Nano, 2026, 20(2): 2510–2522
58. Zhong X, Wang H Y, Zhang C, et al. High-valence metal modulating lattice oxygen in high-entropy layered double hydroxides for enhanced oxygen evolution reaction. Advanced Functional Materials, 2025, 35(47): e72509
59. Pavlovic Z, Ranjan C, van Gastel M, et al. The active site for the water oxidising anodic iridium oxide probed through in situ Raman spectroscopy. Chemical Communications, 2017, 53(92): 12414–12417
60. Ma H, Chen W, Fan Q, et al. Regulating Sn self-doping and boosting solar water splitting performance of hematite nanorod arrays grown on fluorine-doped tin oxide via low-level Hf doping. Journal of Colloid and Interface Science, 2022, 625: 585–595
61. Wang Y, Chan Y S, Zhang R, et al. Insights into the contribution of oxygen vacancies on CO_2 activation for dry reforming of methane over ceria-based solid solutions. Chemical Engineering Journal, 2024, 481: 148360